Supporting information

Influence of Strong π-Acceptor Ligands on Cr-K-edge X-Ray Absorption Spectral Signatures and Consequences on Interpretation of Surface Sites in the Phillips Catalyst.

Yuya Kakiuchi,[a] Svetlana Shapovalova,[b] Bogdan Protsenko,[b] Sergey Guda,[b,c] Olga V. Safonova,[d] Alexander Guda[b,*] and Christophe Copéret[a,*]

E-mail: ccoperet@inorg.chem.ethz.ch; guda@sfedu.ru

[a] ETH Zürich, Vladimir-Prelog-Weg 2, 8093 Zürich, Switzerland

[b] The Smart Materials Research Institute, Southern Federal University, Rostov-on-Don, Russia 344090

[c] Institute of Mathematics, Mechanics and Computer Science,Southern Federal University, Rostov-on-Don, Russia 344090

[d] Paul Scherrer Institute, 5232 Villigen, Switzerland

Table of contents

1. General considerations

All manipulations involving air- and moisture-sensitive compounds were carried out under argon using the standard Schlenk techniques or an argon-filled glovebox. $[Cr(TBOS)_2]_2$[1] (TBOS = tris(tert-butoxy)siloxy), $Cr(TBOS)_3(thf)_2$[2] and $Cr(OAr)_2(thf)_2$[3] (Ar = 2,6-(^{t}Bu)$_2$C$_6$H$_3$) were prepared according to the literature procedure. *N*-Pentane, toluene, THF, DCM were dried by passage through double M-Braun SPS alumina solvent purification columns, and further degassed by 3 Freeze-pump-thaw cycles. All solvents were stored over activated 4 Å molecular sieves (Merck) prior to use, which were activated overnight at 320 °C under high vacuum (10^{-5} mbar). Deuterated benzene was vacuum distilled from purple Na(0)/benzophenone. 2,6-dimethyl isocyanide (XyNC) was purchased from Sigma-Aldrich and used without further purification. Solution ^{1}H NMR spectra were recorded in Teflon J. Young valve-sealed NMR tubes on Bruker 300 MHz spectrometers and the chemical shifts are referenced relative to the solvent.[4] Magnetic susceptibity was determined by Evans method using sealed capillary containing solvent as a reference.[5–8] Transmission infrared spectra were recorded on a Bruker Alpha FT-IR spectrometer equipped with a RockSolid interferometer, DTGS (deuterated triglycine sulfate) detector, and a SiC globar source. A typical experiment consisted of 32 scans in the region between 4000 and 400 cm^{-1}. For single crystal X-ray diffraction analysis, suitable crystals were placed onto MiTeGen loop pins coated in paratone oil and mounted under a flow of nitrogen at 100 K on a Rigaku Synergy S diffractometer with CCD area detector using Cu Kα irradiation. Using Olex2[9], the structures were solved with SHELXT[10] structure solution program and refined using SHELXL[10]. All non-hydrogen atoms were refined with anisotropic displacement parameters. Hydrogen atoms were placed in ideal positions and refined as riding atoms. Elemental Analyses of molecular complexes were provided by the in-house Molecular and Biomolecular Analysis Service (MoBiAS) of ETH Zürich.

2. Synthesis and characterization of molecular Cr-isocyanide adducts

*Elemental analysis was conducted for each of complex, while constantly giving the slightly lower values than expected. While we were not able to clarify the origin of the matter, we decided to report the value as obtained.

2.1. Preparation procedures

$Cr(OAr)_2(XyNC)_2$ (Ar = 2,6-(^{t}Bu)$_2$C$_6$H$_3$) (**1**): $Cr(OAr)_2(thf)_2$ (120 mg, 0.25 mmol) was dissolved in C_6H_6 (10 mL). A C_6H_6 solution of XyNC (66.2 mg, 0.505 mmol, 2.02 equiv) was added to the Cr solution at room temperature, giving a yellow suspension. The reaction mixture was stirred overnight (16h). All the volatiles were removed under vacuum, yielding a yellow powder. The thus-obtained yellow powder was washed with *n*-pentane (3 mL x 3 times). The powder product was dried under vacuum to give desired product as yellow powder in 85% yield. XRD-quality crystal was obtained by recrystallization from consentrated DCM solution at -30 °C. Elemental analysis for $C_{46}H_{60}N_2O_2Cr$: expected 76.21% C, 8.34% H, 3.86% N; found: 75.52% C, 8.12% H, 3.85% N. ^{1}H NMR (300 MHz, THF-d_8) δ/ppm =17.70 (br., $\nu_{1/2} \approx 200$ Hz), 7.10 (br., $\nu_{1/2} \approx 30$ Hz), 6.72 (br., $\nu_{1/2} \approx 30$ Hz), 6.04 (br., $\nu_{1/2} \approx 30$ Hz), 1.41 (br., $\nu_{1/2} \approx 25$ Hz), -4.40 (br., $\nu_{1/2} \approx 220$ Hz). $M_{eff} = 5.46\ \mu_B$.

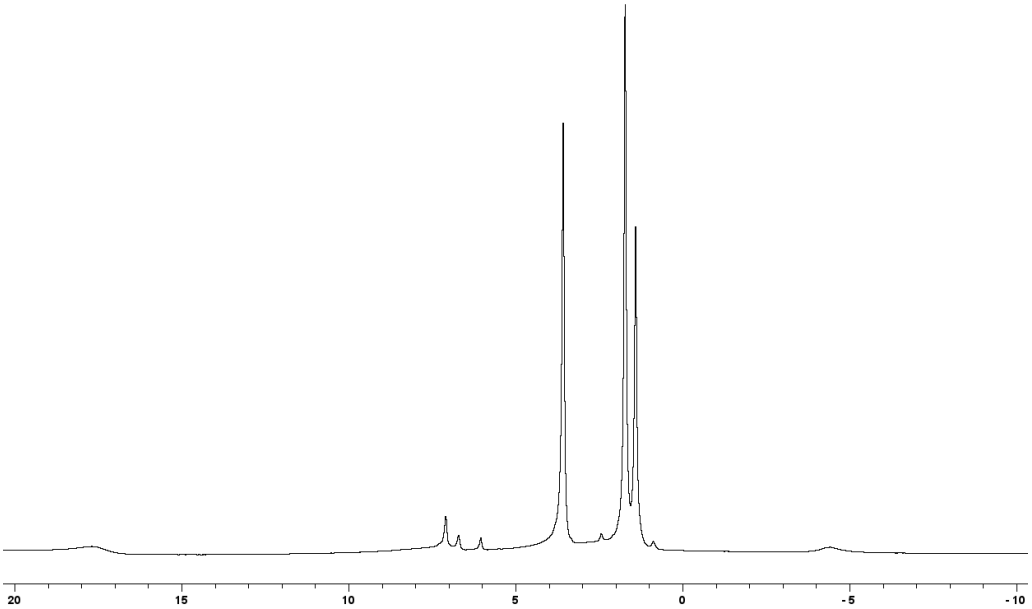

Figure S1. ^{1}H NMR spectrum of $Cr(OAr)_2(XyNC)_2$ (**1**) in THF-d_8.

Cr(Osi(O*t*Bu)$_3$)$_2$(XyNC)$_4$ (2): $[Cr(OSi(OtBu)_3)_2]_2$ (150 mg, 0.130 mmol) was dissolved in toluene (5 mL), giving a pale blue solution. A toluene solution (2 mL) of XyNC (136.0 mg,

1.04 mmol, 8 equiv) was added to the Cr solution at room temperature, immediately giving an intense red solution. The mixture was stirred for 1 h. All the volatiles were removed under vacuum, leaving a red powder. Recrystallization from minimal amount of *n*-pentane at -30 °C afforded red crystals in 77% yield. The obtained crystal was directly used for sc-XRD analysis. Elemental analysis for $C_{60}H_{94}N_4Osi_2Cr$: expected 65.30 % C, 8.22 % H, 5.08% N; found: 64.53% C, 8.18% H, 5.01% N. ^{1}H NMR (300 MHz, C_6D_6) δ/ppm = 7.88 (br., $\nu_{1/2} \approx 27$ Hz, 8H), 5.78 (br., $\nu_{1/2} \approx 200$ Hz, 24H), 3.02 (br., $\nu_{1/2} \approx 28$ Hz, 4H), 1.67 (br., $\nu_{1/2} \approx 235$ Hz, 54H). μ_{eff} = 3.04 μ_B.

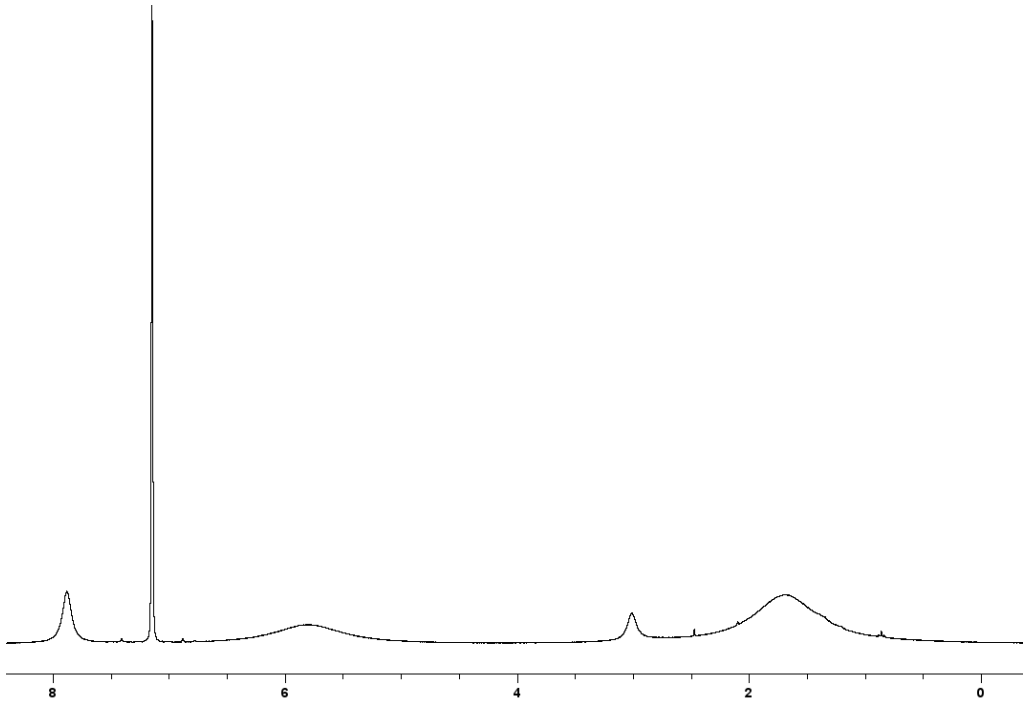

Figure S2. ^{1}H NMR spectrum of $Cr(OSi(O\mathit{t}Bu)_3)_2(XyNC)_4$ (**2**) in C_6D_6.

$Cr(OSi(O\mathit{t}Bu)_3)_3(XyNC)_2$ (3): $Cr(OSi(OtBu)_3)_3(thf)_2$ (150 mg, 0.150 mmol) was dissolved in toluene (5 mL), giving a pale blue solution. A toluene solution (2 mL) of XyNC (40.0 mg, 0.305 mmol, 2 equiv) was added to the Cr solution at room temperature, giving a blue solution. The mixture was stirred overnight (16 h). All the volatiles were removed under vacuum, leaving a pale blue powder.

Recrystallization from minimal amount of *n*-pentane at -30 °C afforded a deep blue crystal in 78% yield. The obtained crystal was directly used for sc-XRD analysis. Elemental analysis for $C_{54}H_{99}N_2O_{12}Si_3Cr$: expected 58.72 % C, 9.03 % H, 2.54%; found: 57.72% C, 9.23% H, 2.24% N. ^{1}H NMR (300 MHz, C_6D_6) δ/ppm = 12.56 (br., $\nu_{1/2} \approx 100$ Hz), 11.82 (br., $\nu_{1/2} \approx 170$ Hz), 8.52 (br., $\nu_{1/2} \approx 600$ Hz), 1.82 (br., $\nu_{1/2} \approx 350$ Hz), -0.94 (br., $\nu_{1/2} \approx 120$ Hz), -2.17 (br., $\nu_{1/2} \approx 100$ Hz),) . $\mu_{eff} = 3.92\ \mu_B$.

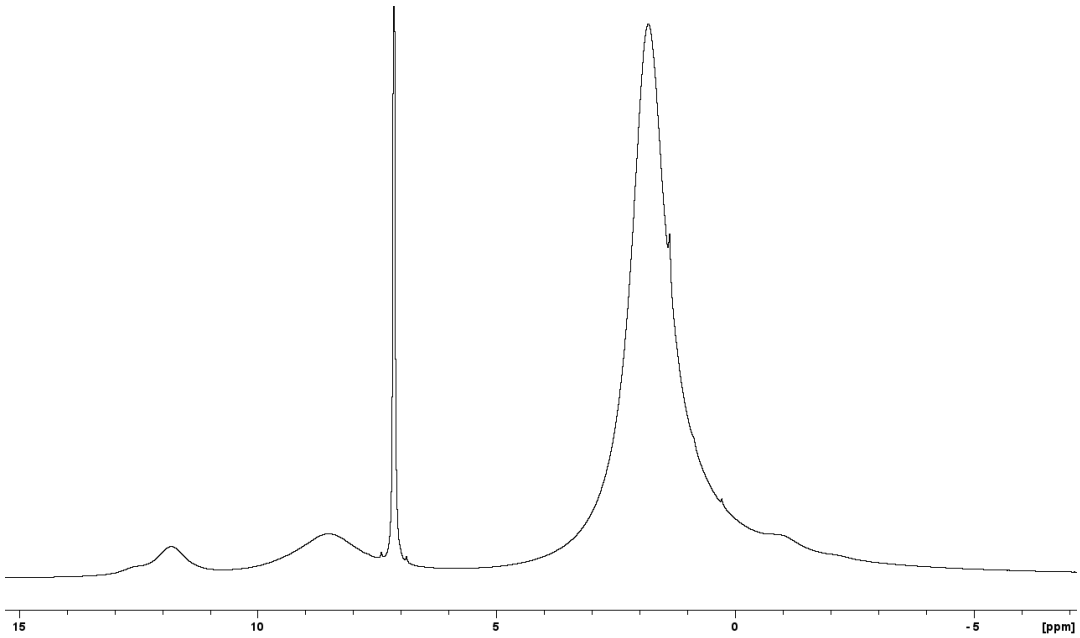

Figure S3. ^{1}H NMR spectrum of $Cr(OSi(OtBu)_3)_3(XyNC)_2$ (**2**) in C_6D_6.

2. 2. Single-crystal X-ray diffraction analysis

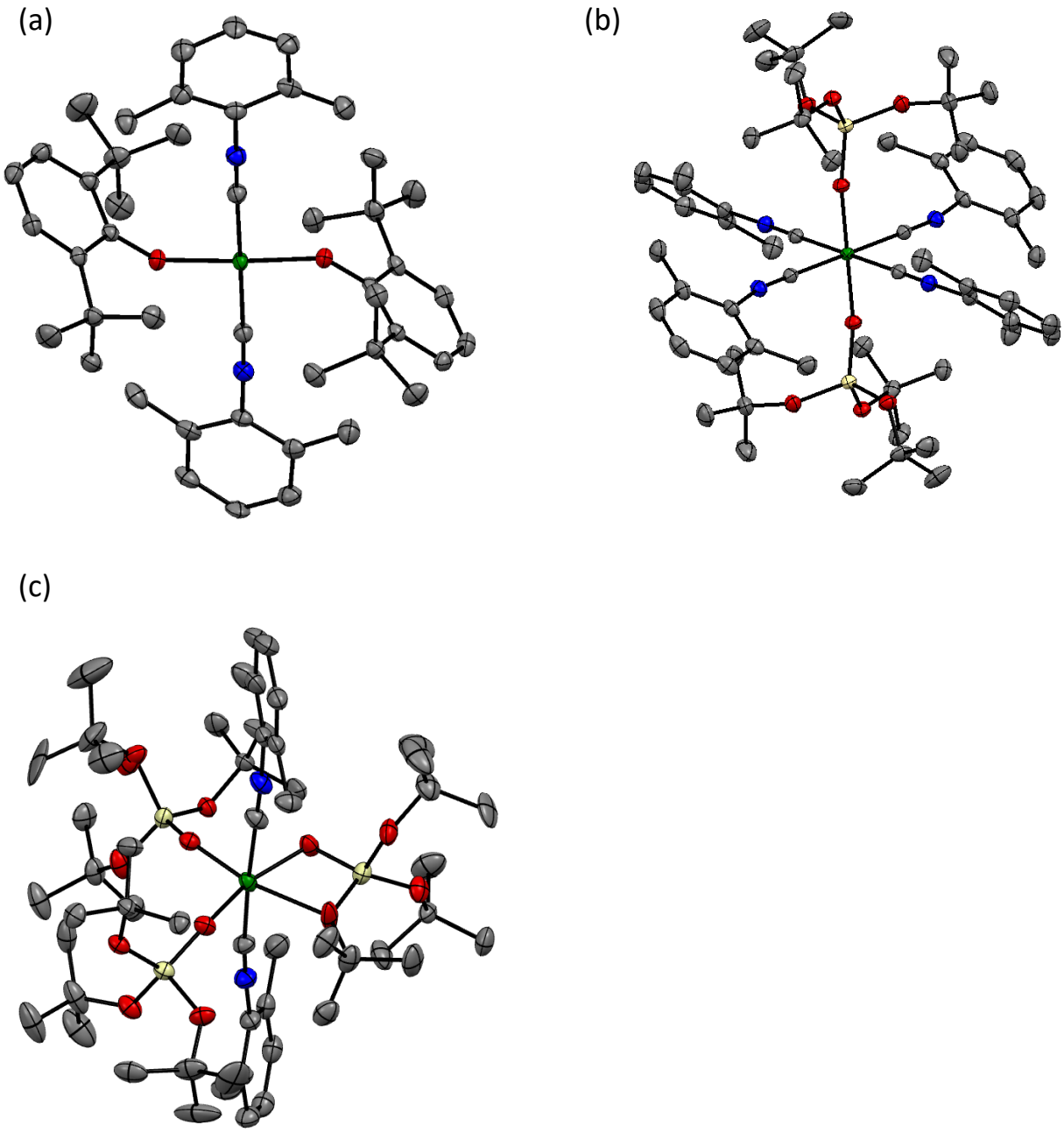

Figure S4. Molecular structure of (a) $Cr(OAr)_2(XyNC)_2$ (**1**), (b) $Cr(TBOS)_2(XyNC)_4$ (**2**) and (c) $Cr(TBOS)_3(XyNC)_2$ (**3**) with 50% thermal elipsoids. All hydrogen atoms were omitted for clarity.

Table S1. Crystal data and data collection parameters of $Cr(OAr)_2(XyNC)_2$ (1), $Cr(TBOS)_2(XyNC)_4$ (2) and $Cr(TBOS)_3(XyNC)_2$ (3)

	$Cr(OAr)_2(XyNC)_2$ (**1**)	$Cr(TBOS)_2(XyNC)_4$ (**2**)	$Cr(TBOS)_3(XyNC)_2$ (**3**)
empirical formula	$C_{46}H_{60}N_2O_2Cr$	$C_{60}H_{90}N_4O_8Si_2Cr$	$C_{54}H_{99}N_2O_{12}Si_3Cr$
formula weight	724.96	1103.53	1104.62
crystal system	Monoclinic	Triclinic	Orthorhombic
space group	*P2₁/c*	*P-1*	*P2₁2₁2₁*
a, Å	10.9280(4)	11.3465(2)	13.1907(3)
b, Å	28.6868(10)	12.5357(2)	20.8362(5)
c, Å	14.0779(6)	13.0549(2)	23.4449(6)
α, deg.	90	109.944(2)	90
β, deg.	110.037(5)	101.7450(10)	90
γ, deg.	90	105.8320(10)	90
V, Å^3	4146.1(3)	1586.41(5)	6443.7(3)
Z	4	1	4
$D_{calcd,}$ g/cm^3	1.161	1.155	1.139
μ [Cu-Kα], mm^{-1}	2.550	2.258	2.429
T, K	100.0	100.0	100.0
crystal size, mm	0.3 × 0.2 × 0.05	0.2 x 0.2 x 0.05	0.3 x 0.2 x 0.05
2θ range for data collection (deg.)	6.162 to 161.68	7.626 to 160.538	5.674 to 161.742
no. Of reflections measured	61380	24416	47345
unique data (R_{int})	8955 (0.0565)	6771 (0.0263)	13511 (0.0546)
data / restraint / parameters	8955/15/700	6771 / 0 / 520	13511 / 773 / 804
*R*1 ($I > 2.0\sigma(I)$)	0.0618	0.0322	0.0835
*wR*2 ($I > 2.0\ \sigma(I)$)	0.1456	0.1089	0.1905
*R*1 (all data)	0.0680	0.0336	0.0854
*wR*2 (all data)	0.1488	0.1118	0.1915
GOF on F^2	1.108	0.996	1.104
Δρ, e Å^{-3}	0.76 / -0.53	0.33 / -0.52	0.40 / -1.07

a) $R1 = (\Sigma||Fo| - |Fc||)/(\Sigma\ |Fo|)$ b) $wR2 = [\{\Sigma\ w(Fo^2-Fc^2)^2\}/\{\Sigma\ w(Fo^4)\}]^{1/2}$

2. 3. IR spectra

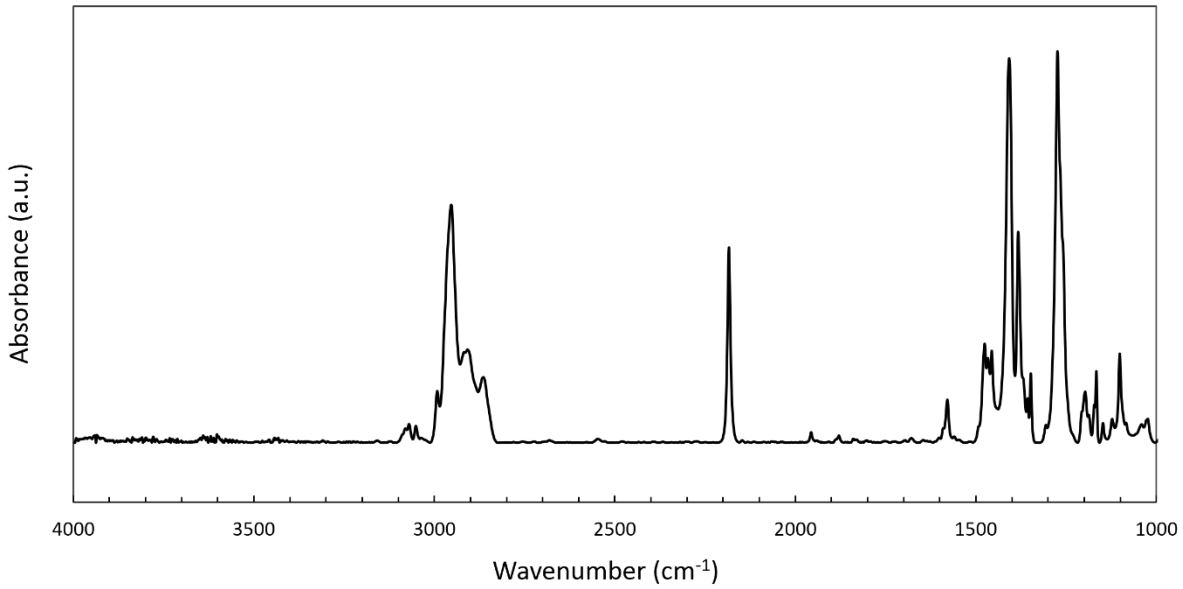

Figure S5. IR spectrum of $Cr(OAr)_2(XyNC)_2$ (**1**).

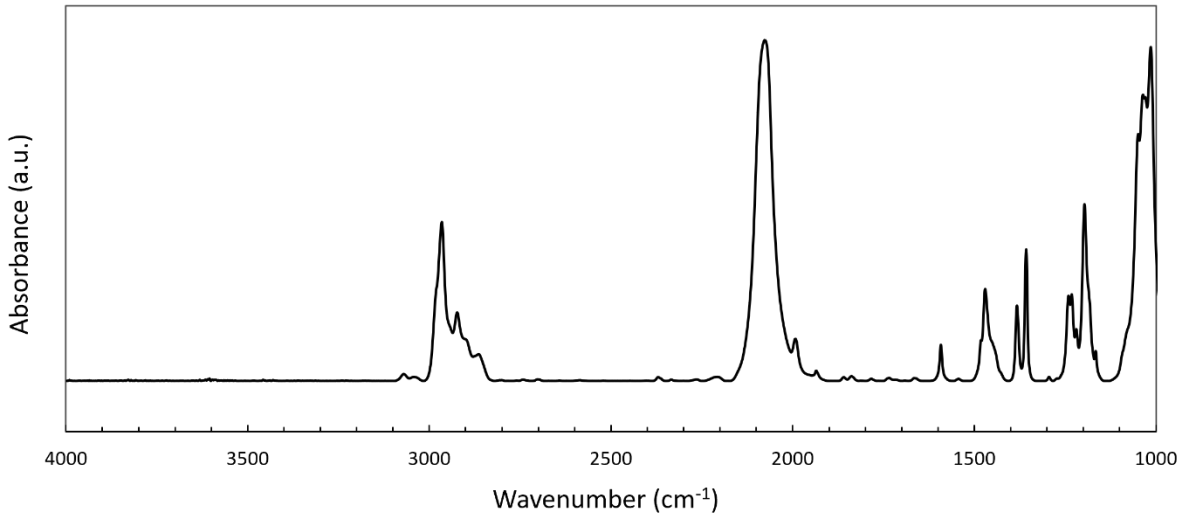

Figure S6. IR spectrum of $Cr(TBOS)_2(XyNC)_4$ (**2**).

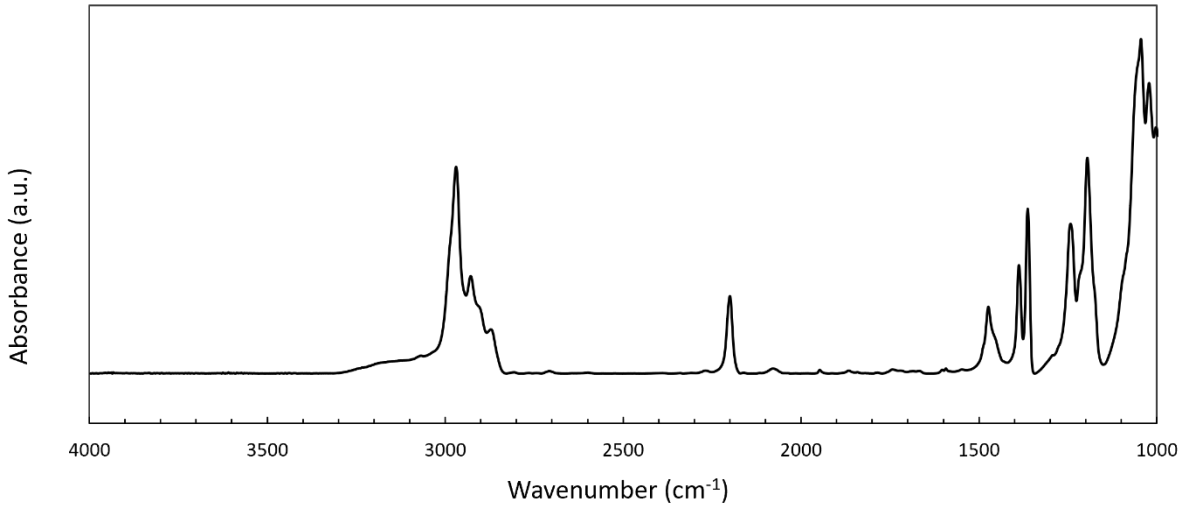

Figure S7. IR spectrum of $Cr(TBOS)_3(XyNC)_2$ (**3**).

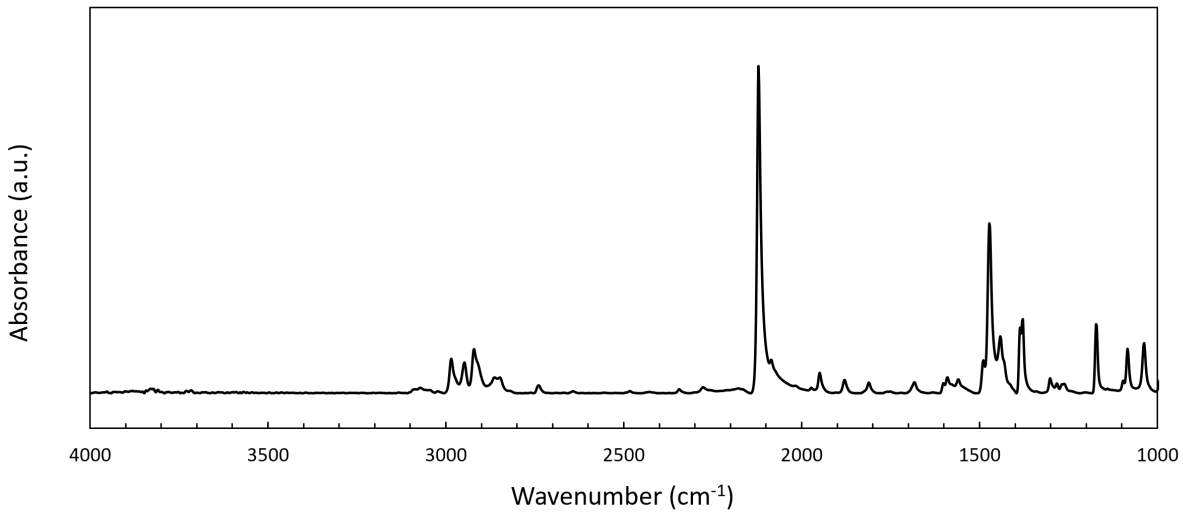

Figure S8. IR spectrum of XyNC.

3. Experimental setup for Cr K-edge XAS spectra of molecular library

XAS measurements were carried out at the Cr K-edge at the SuperXAS beamline at the Swiss Light Source (SLS) (PSI,Villigen, Switzerland). The storage ring was operated at 2.4 GeV in top-up mode with a ring current of around 400 mA. The incident photon beam provided by a 2.9 T super bend magnet source was selected by a Si (111) quick-EXAFS monochromator and the rejection of higher harmonics and focusing were achieved by a rhodium-coated collimating mirror at 2.8 mrad and a rhodium-coated torroidal mirror at 2.8 mrad. The beam size on the sample was 100 x 100 μm. During measurement, the monochromator was rotating with 10 Hz frequency in 2 deg angular range and X-ray absorption spectra were collected in transmission mode using ionization chambers filled with He-N_2 gas mixtures, specially developed for quick data collection with 1 MHz frequency. The beamline energy was calibrated with a Cr reference foil to the Cr K-edge position at 5989.0 eV. To avoid contact with air, all samples were sealed in quartz capillaries (0.01 mm wall thickness, 0.9 mm outer diameter; Hilgenberg GmbH) under inert atmosphere and measured as a capillary. Opening of the capillaries, filled with samples, were sealed with Apiezon vacuum grease and wax, followed by further sealing with epoxy adhesive (®LOCTITE EA3450, purchased from Henlel Adhedive Technologies). The the sealed capillaries were further stored in glass tubes under argon atmosphere and opened just before the measurement. Energy calibration, background subtraction and normalization was performed in the Athena program from IFEFFIT package.[11,12] The energy alignment of the spectra was performed using metal foil of Cr as a reference. XAS spectra for $[Cr(TBOS)_2]_2$[3], $Cr(TBOS)_3$[3], $Cr(POSS)(thf)_3$[3] and activated Phillips catalyst (at 300K and 100K)[13] were taken from literature.

4. Cr K-edge XAS spectra and theoretical simulations

4.1. Computational Details

Geometry optimization and electronic structure calculations were performed within density functional theory (DFT) in AMS-2022 program package.[14] A benchmark set of geometries, energies, charges and spectra was carried out for the six-coordinated complex **2** using revPBE[15], hybrid B3LYP[16,17], meta-GGA TPSS[18], BLYP[16,19] and M06[20] level of theory with DFT-D3[21] dispersion corrections and Becke–Johnson damping[22] (D3(BJ)) functionals. We used the triple-ζ basis set with one polarization function (TZP) for geometry optimization and quadruple-ζ basis set with four polarization functions (QZ4P) for charge analysis and pre-edge spectra calculations. Cr K-edge XANES spectra were simulated within two approximations. The first one is based on DFT molecular orbitals (DFT-MO) and corresponding dipole and quadrupole matrix elements between Cr 1s core and unoccupied states. This approach was applied for the pre-edge region and visualization of corresponding molecular orbitals. In the second approach the wider energy region of spectrum is calculated with finite difference method, implemented in the FDMNES code.[23] The finite difference grid with 0.2 Å interpoint distance was constructed inside a sphere with 5.5 Å radius around absorbing Cr. Theoretical spectra were further convoluted to account for the corehole lifetime broadening and instrumental energy resolution (arctangent function was used to model the energy dependence of the Lorentzian width).

4.2 Calculation benchmark: Comparison of experimental- vs. calculated spectra

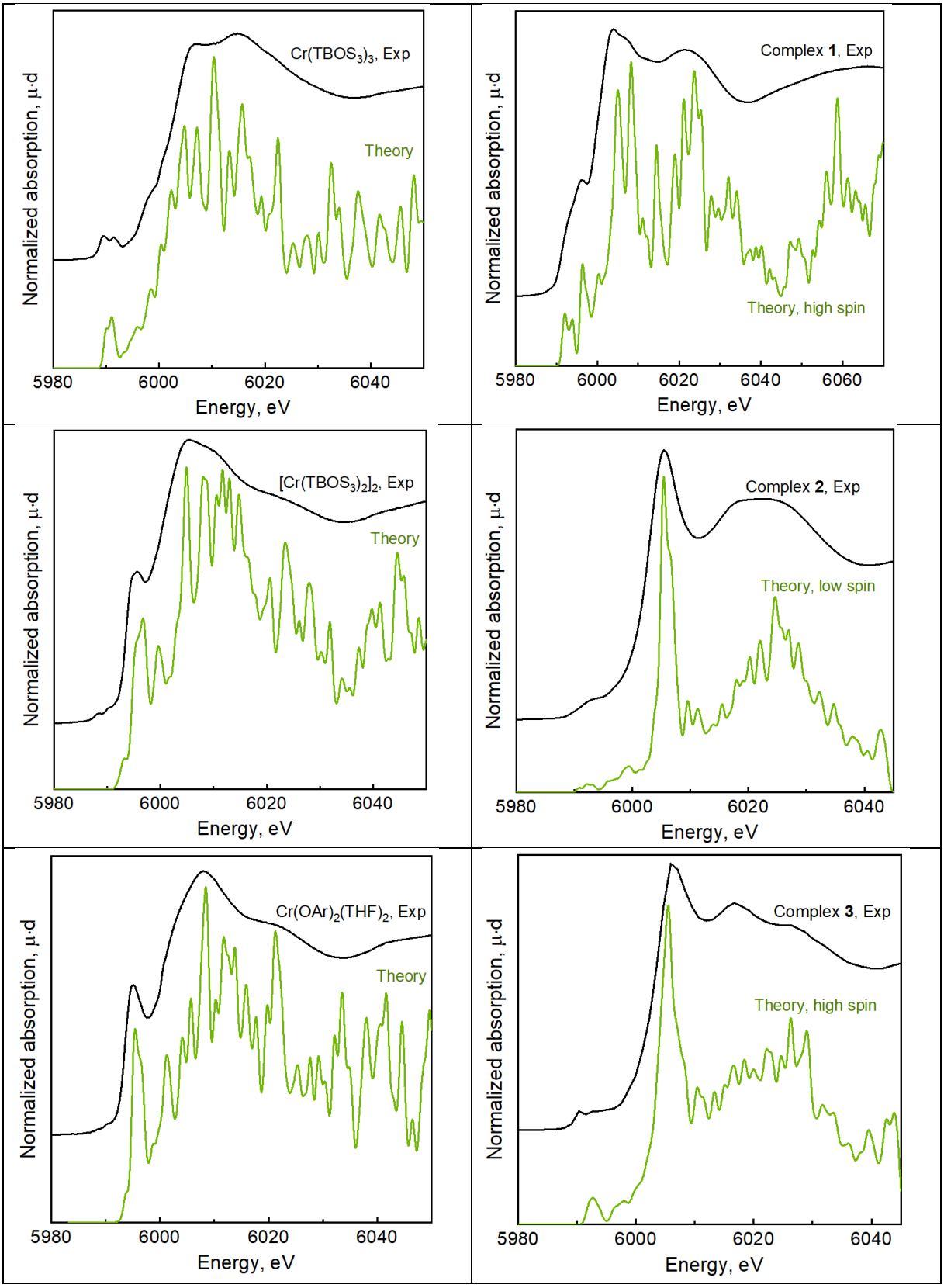

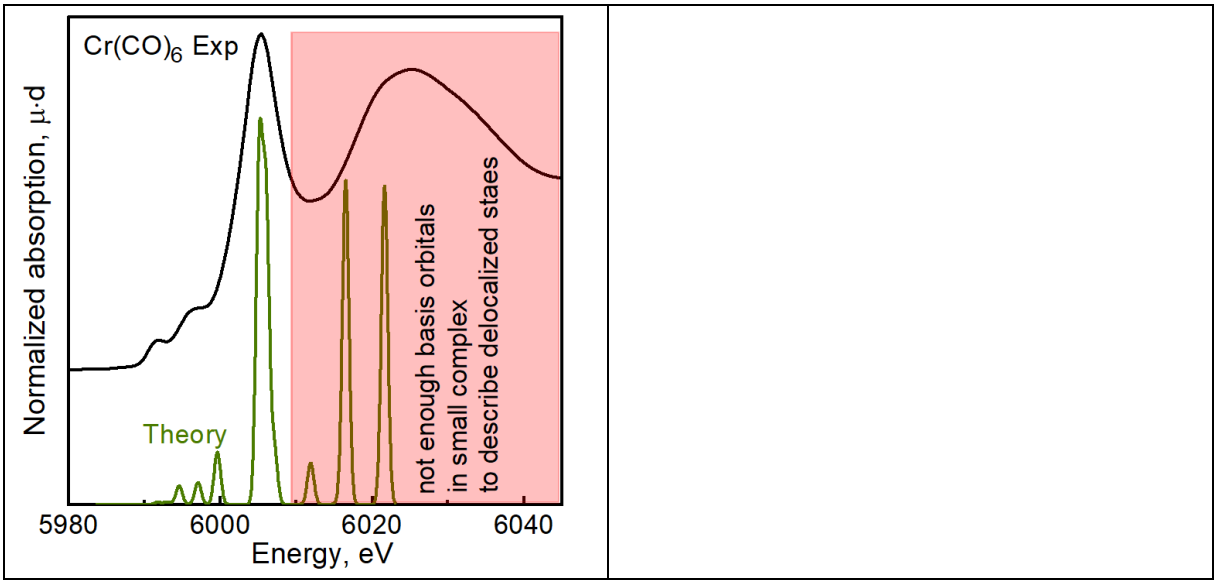

Figure S9. Benchmark TD-DFT calculations within the molecular orbital approach (AMS-2022 software) for studied complexes.

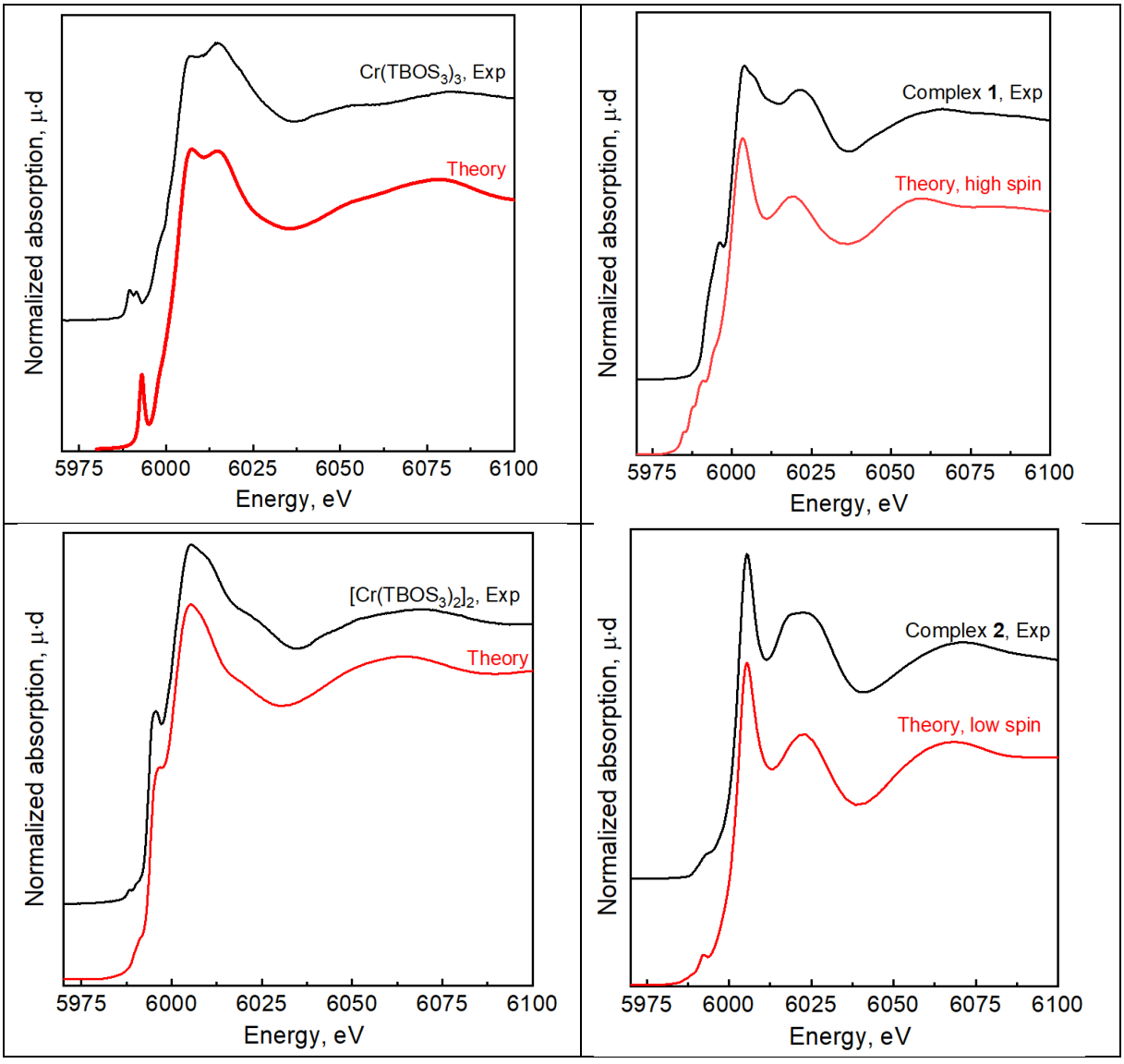

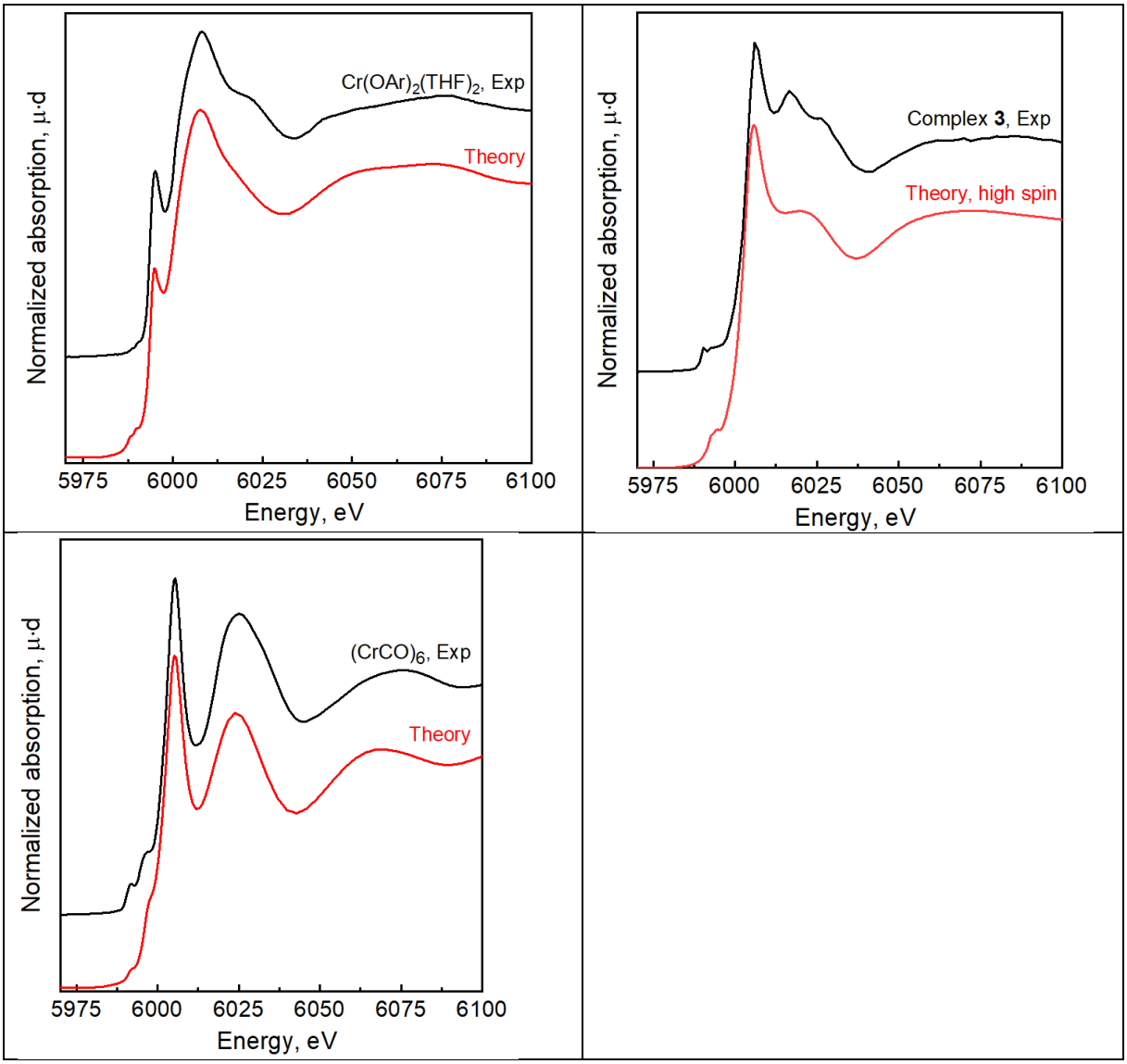

Figure S10. Benchmark calculations within the finite difference method (FDMNES software) for the studied complexes.

4.3 Justification of using isocyanide ligands as substitution for carbonyls: Comparison of their effect on Cr K-edge XAS

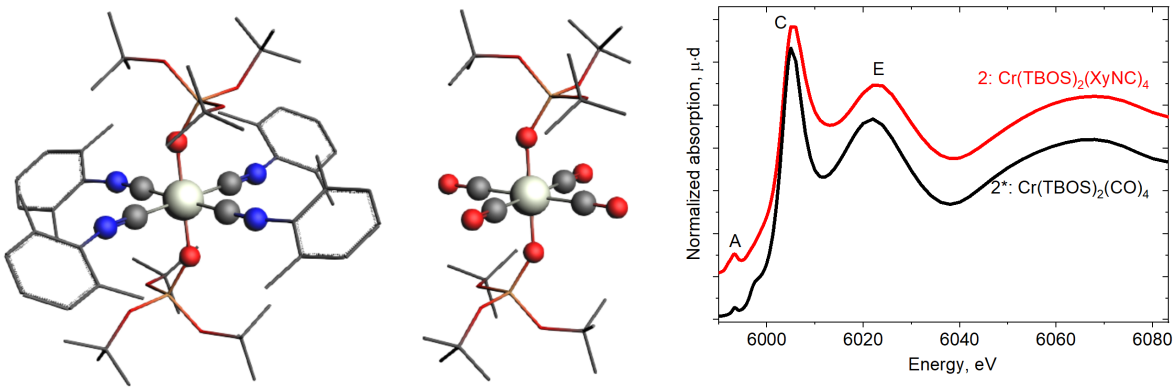

Figure S11. The similarity of spectra for complexes with isocyanide and carbonyl ligands. Theoretical spectra for complex 2 compared to its structural analogue but with CO replacing XyNC.

4.4. Ambiguity of the naive chemical shift analysis applied to absorption edge of the complexes with isocyanide and carbonyl ligands

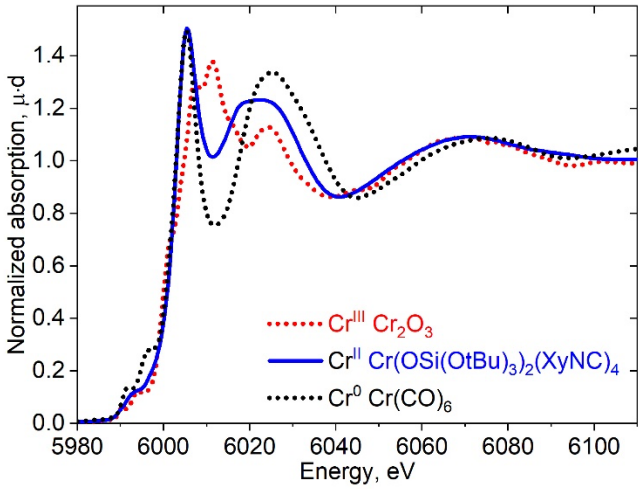

Figure S12. Overlap of the absorption edge positions between Cr^0, Cr^{II} and Cr^{III} references: oxide Cr_2O_3, and Cr^0 and Cr^{II} complexes with carbonyl and isocyanide ligands

4.5. Spectral changes upon substitution of THF with isocyanide ligands (supplementary to the Figure 1 in the main text)

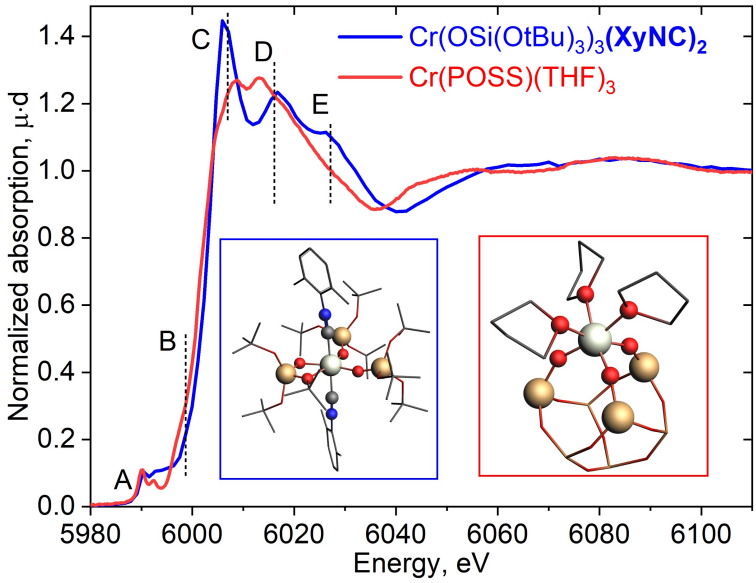

Figure S13. Experimental Cr K-edge XANES spectra for octahderal Cr(III) siloxide complexes with isocyanide (for **3**) and comparison with Cr(POSS)(thf)$_3$ (= [(cC$_5$H$_9$)$_7$Si$_7$O$_9$(O)$_3$Cr(thf)$_3$])representing O-based enironment.

4.6. EXAFS analysis for complex 2.

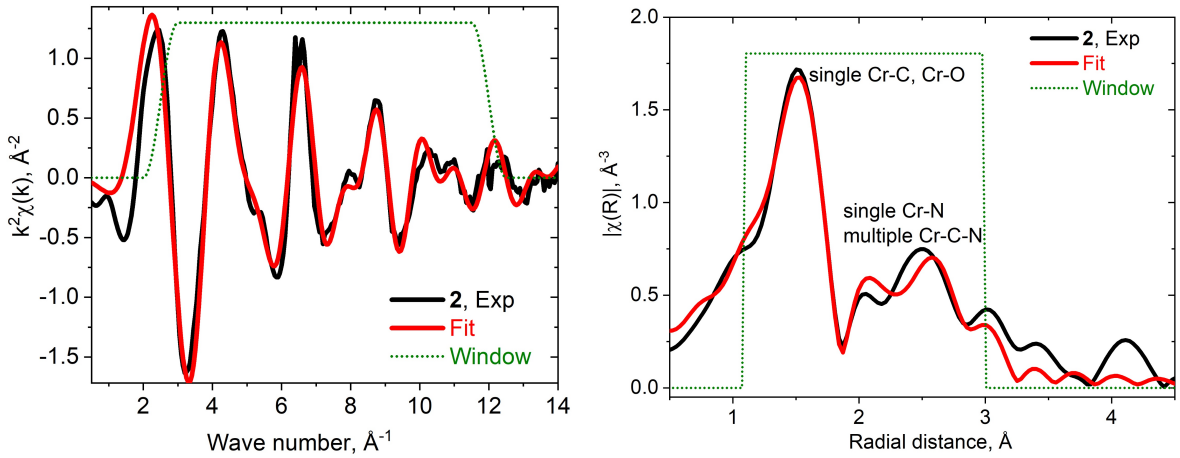

Figure S14. Experimental data and theoretical fit for complex 2. Left panel: EXAFS oscillations above the Cr K-edge. Right panel: Amplitude of the Fourier transformed $k^2\chi(k)$ signal.

Table S2. Atomic coordination shells used in the EXAFS fit for **2** (ranges k=3…12 Å^{-1}, R = 1.1…3 Å for $k^2\chi(k)$ data) and corresponding parameters. Number of independent parameters during the fit was N_{ind} = 11.3, number of variables N_{var} = 7. Resulting R-factor = 0.012.

Atom	S_0^2	CN (constrained)	σ^2	E_0	R, Å
O ($OSi(OtBu)_3$)	0.85	2	0.006 ± 0.002	-0.25	1.94 ± 0.01
C (XyNC)		4	0.002 ± 0.001		2.03 ± 0.02
N (XyNC)					3.20
C-N					
C-N-C					

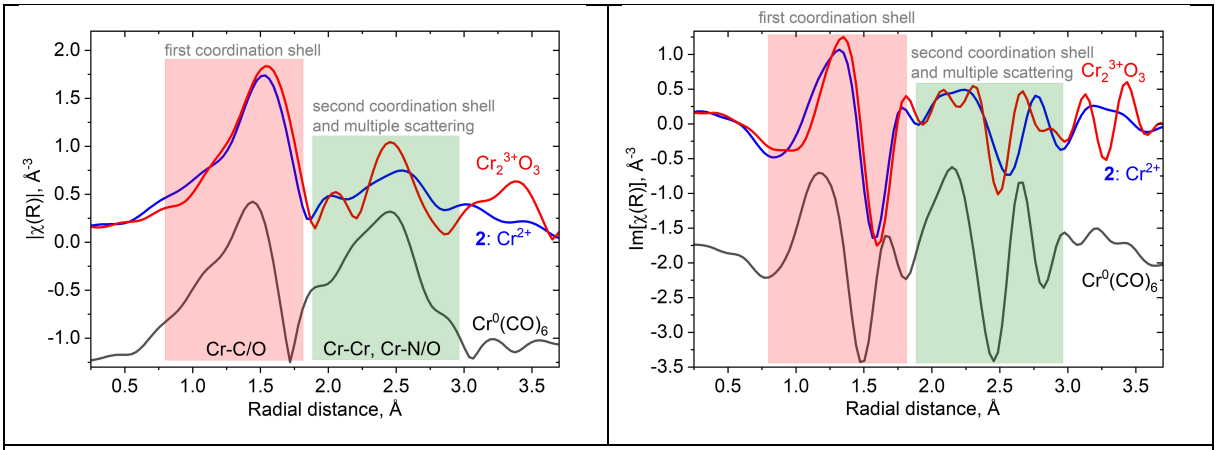

Figure S15. Magnitude and imaginary part of the Fourier transformed EXAFS signal for octahedral molecular complex **2** with four isocyanides, bulk oxide Cr_2O_3 and chromium carbonyl.

In some cases an inspection to the Im(FT) reveals the occurrence of overlap between different contributions falling in the same R range. In Figure S15 we demonstrate the similarity between FT signal from Cr_2O_3 ane **2** at 2…2.5 A.

4.7. Benchmark of different exchange correlation functionals

Table S3. Results of the benchmark test for complex **2**: distances (Å) for different Vxc and spin states (in a high spin state CrII has 4 unpaired electrons and in a low spin – 2 unpaired electrons)

		revPBE-D3(BJ)		**B3LYP-D3(BJ)**		**TPSS-D3(BJ)**		**TPSS**		**BLYP-D3(BJ)**	
	cif	**HS**	**LS**	**HS**	**LS**	**HS**	**LS**	**HS**	**LS**	**HS**	**LS**
Cr-C2	2.024 (11)	2.123	1.978	2.140	2.019	2.125	1.983	2.311	2.007	2.062	1.997
Cr-C3	2.019 (12)	2.040	1.966	broken bond	2.006	2.044	1.980	2.151	2.007	broken bond	1.984
Cr-C4	2.024 (11)	2.273	1.978	2.154	2.019	2.211	1.983	2.187	2.007	2.102	1.996
Cr-C5	2.019 (12)	2.077	1.966	broken bond	2.006	2.086	1.980	2.088	2.007	2.110	1.984
Cr-O10	1.930 (8)	1.937	1.941	1.934	1.935	1.919	1.925	1.962	1.957	1.940	1.942
Cr-O12	1.930 (8)	1.950	1.941	1.947	1.935	1.933	1.926	1.943	1.957	1.948	1.942

Table S4. Results of the benchmark test of C≡N bonds distances (Å) for complexes **1, 2, 3**

	Free isocyanide ligand	1		2		3	
		HS	LS	HS	LS	HS	LS
B3LYP-D3(BJ)	1.171	1.160 1.160	1.166 1.167	1.167 1.162 1.168 1.162	1.169	1.157 1.161	1.160 1.164
TPSS-D3(BJ)	1.180	1.174 1.176	1.181 1.181	1.180 1.173 1.189 1.172	1.181	1.167 1.171	1.172 1.175
M06	1.169	1.157 1.157	1.165 1.166	1.164 1.160 1.167 1.159	1.168	1.156 1.154	1.162 1.159

The results of DFT calculations for C≡N bondlength in 1, 2 and 3 qualitatively agree with the values from single crystal XRD refinement but underestimate observed in the experiment variations. Shortening of the bondlegth for HS state of 3 is confirmed in DFT/B3LYP, DFT/TPSS and DFT/M06 approaches. For 1 and 2 the calculations predict minor contraction of the C≡N distance, that is smaller in 2 compared to 1. In the crystallographic data the C≡N distance in 1 remains almost unchaged while experiment predicts elongation of bondlegth in 2. We attribute these uncertainties to the effect of packing effect and the level of one-electron approximation, that was sufficient for reproducing Cr K-edge data and distances to the first coordination shell around metal.

4.8. Isocyanide-ligand effect on the Cr K-edge XAS spectrum of Cr(III) complex

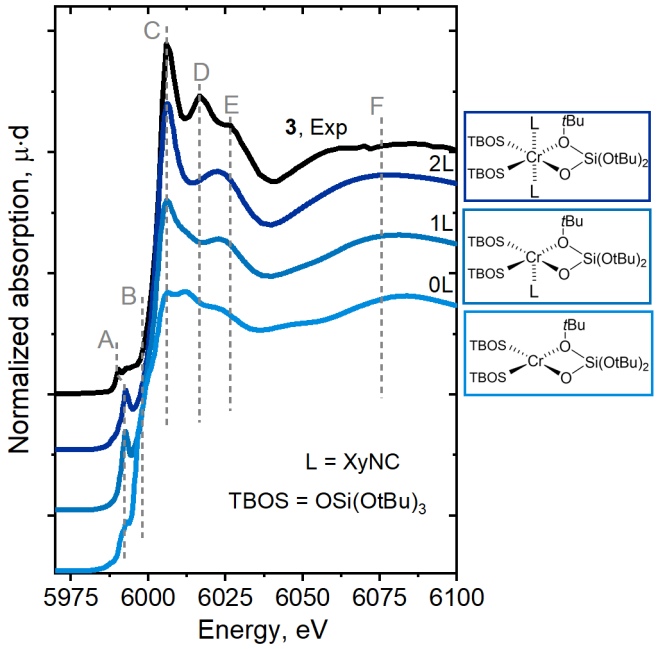

Figure S16. Experimental Cr K-edge XAS spectrum for **3** compared to the series of calculated spectra for $Cr(TBOS)_3(XyNC)_n$ (n = 0 – 2). The structures for different n were obtained by removing XyNC ligands from DFT-optimized $Cr(TBOS)_3(XyNC)_2$ without subsequent relaxation

4.9. Unoccupied molecular orbitals in $Cr(CO)_6$

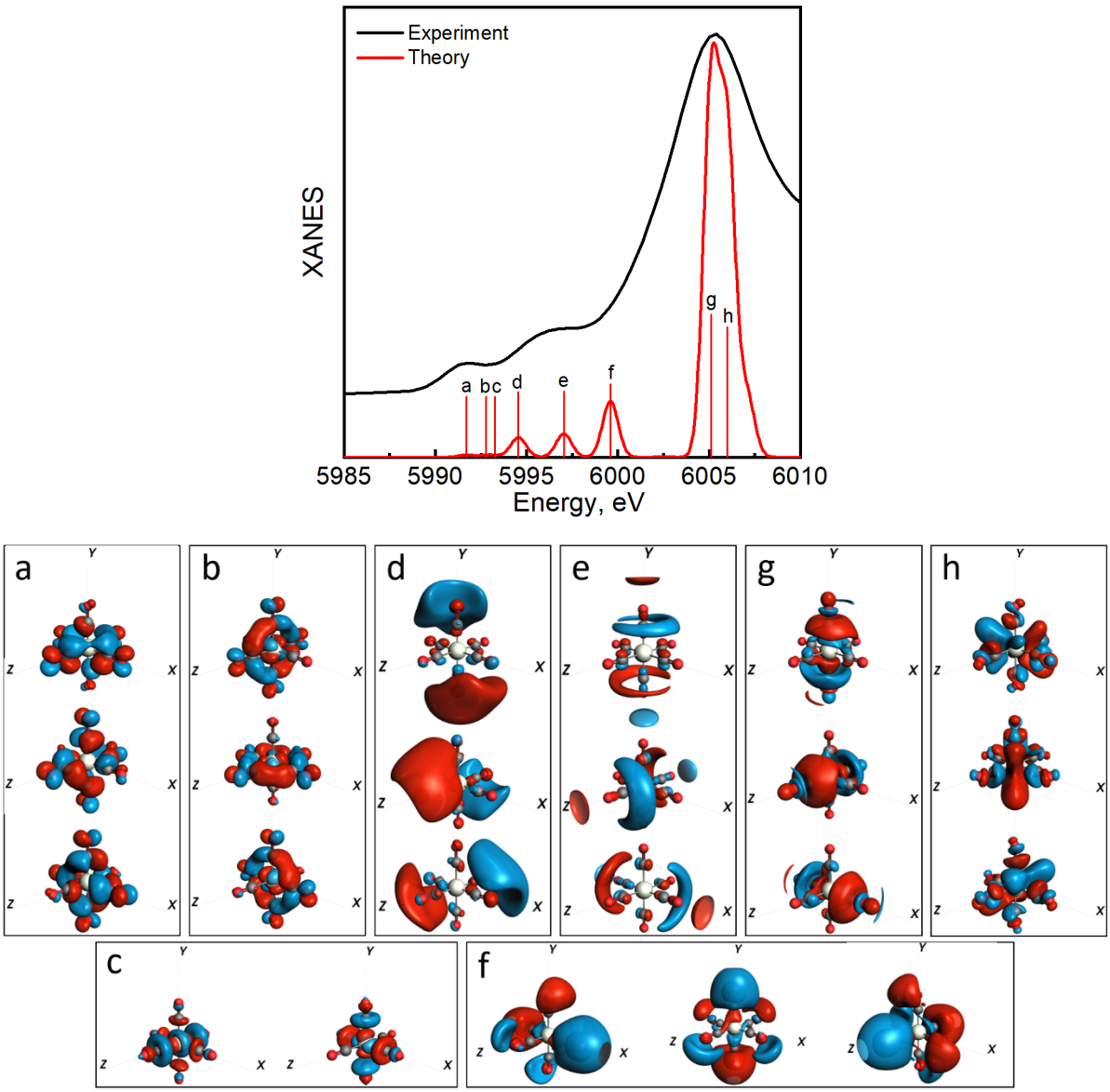

Figure S17. Edge and pre-edge features of $Cr(CO)_6$ and corresponding molecular orbitals

4.10. Orbital analysis on Cr-isocyanide bonding by ETS-NOCV approach

To gain quantitative understanding on the orbital-interaction around Cr-isocyanide bonding, address this question, we refer to the extended transition state – natural orbitals for chemical valence (ETS-NOCV). Such method can be used to analyze the metal-ligand chemical bonds in transition metal complexes and provide quantitative details about ligand-to-metal donation and metal-to-ligand back-donation charge transfer. This method combines the energy decomposition analysis[24] with the natural orbitals for chemical valence (NOCV).[25,26] In NOCV method the electron density rearrangement is defined with respect to the orthonormalized non-interacting fragments.[27] Electron density analysis was performed in the AMS-2022 program package. All complexes were divided by fragments as shown in Figure S18 with different colors.

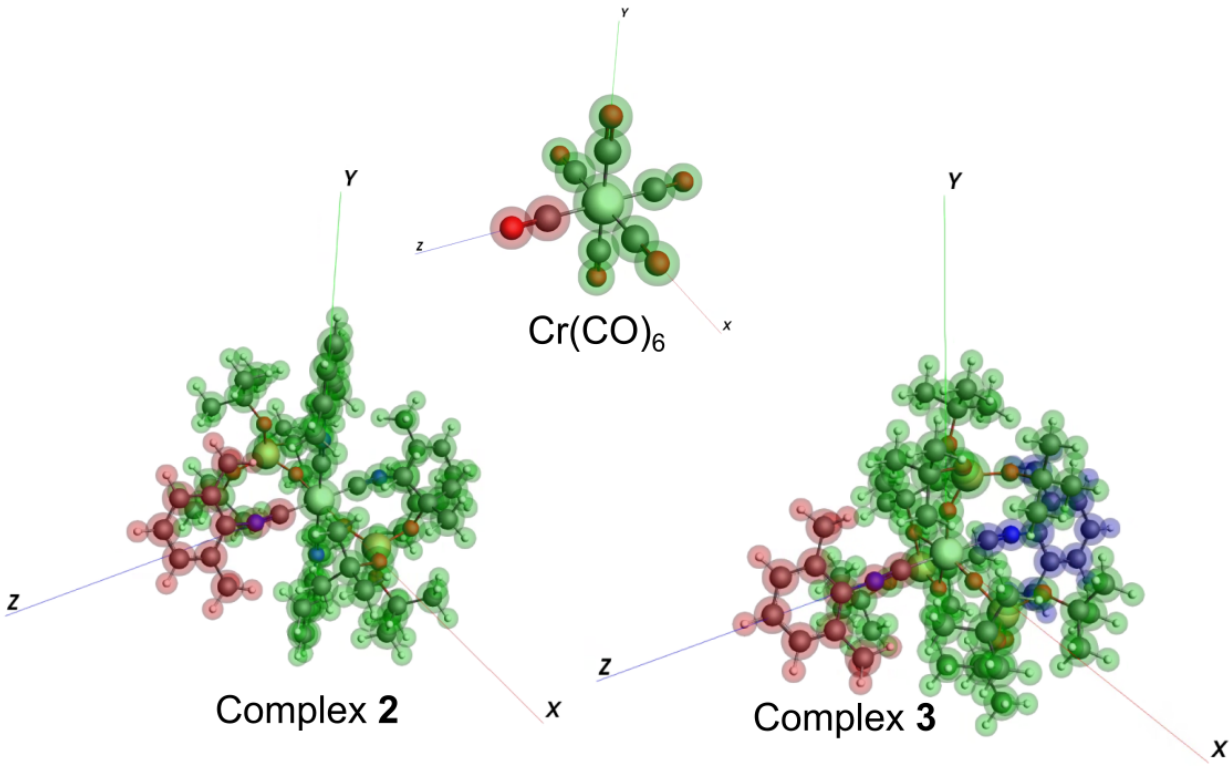

Figure S18. Fragments of $Cr(CO)_6$ and complexes **2**, **3** that were chosen for ETS-NOCV calculations. Parental metal-fragment is shown in green, and additional ligand (CO or isocyanide) are shown in red and blue.

Figure S19 presents the NOCV contours describing the bond between the $Cr(CO)_5$ fragment and the C=O ligand in the $Cr(CO)_6$ complex. There are three orbitals participating in bonding, i.e., exhibiting high eigenvalues. The first isodensity surface is associated with the largest eigenvalue and clearly represents to the σ-ligand-to-metal donation component, while two other orbitals show the metal-to-ligand π-backdonation.

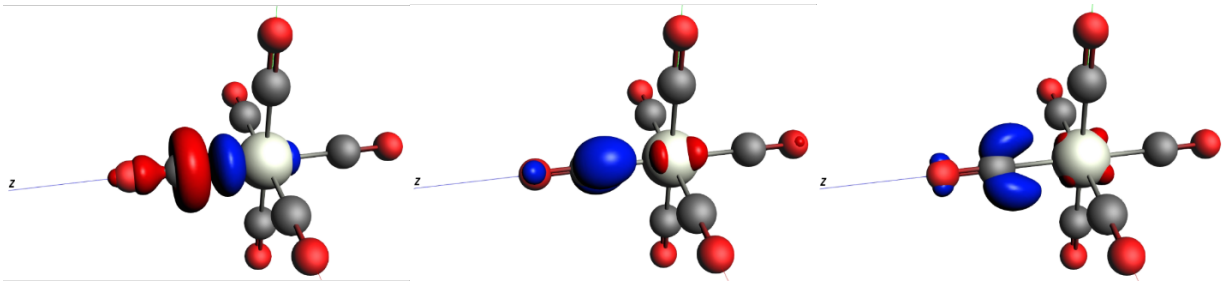

Figure S19. Isosurfaces of the NOCV characterizing the bond between the $Cr(CO)_5$ fragment and the C=O ligand with three highest eigenvalues components (|ν| = 0.525, 0.484, 0.484 from the left to right). The isodensity value is ±0.005 e/au^3. The charge sign is shown with red (negative values) or blue (positive values).

Figure S20 presents the NOCV contours describing the bond between the $Cr(TBOS)_2(XyNC)_3$ fragment and additional XyNC ligand in the complex **2**. Seven orbitals participate in bonding, i.e., exhibit high eigenvalues. The first NOCV $\Delta\rho_1$ in the figure associated with the largest eigenvalue describes a π-back donation between the virtual orbital of XyCN and occupied metal d orbital.

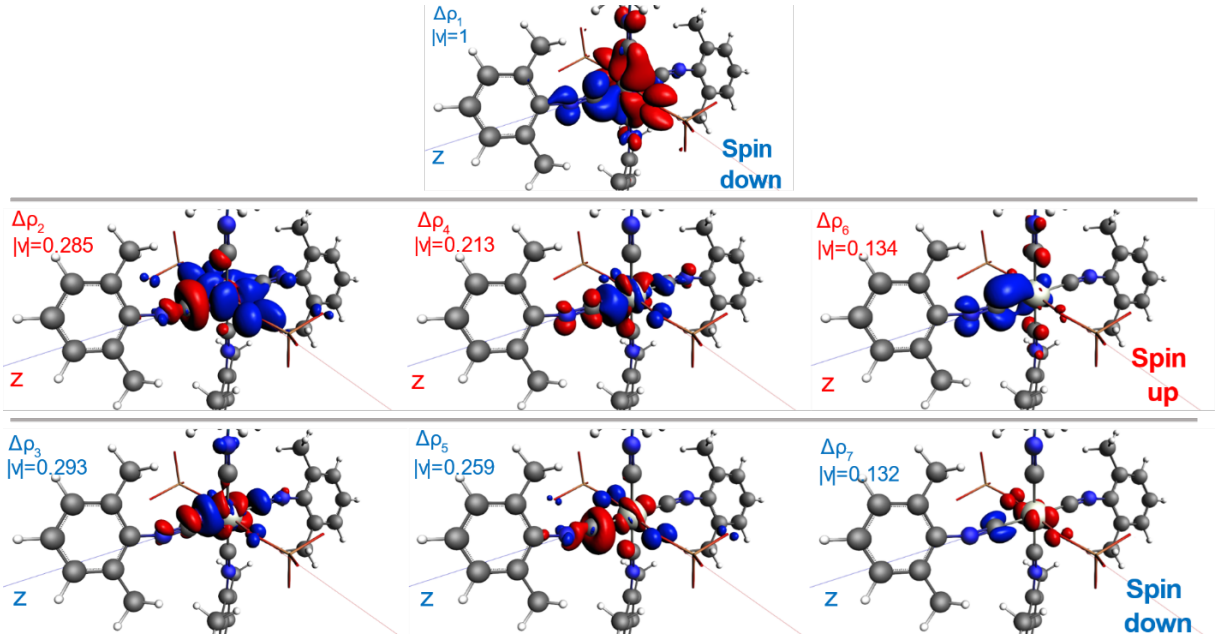

Figure S20. Isosurfaces of the natural orbitals characterizing the bond between the $Cr(TBOS)_2(XyNC)_3$ fragment and additional XyCN ligand. The seven highest eigenvalues components (|ν| values) are depicted with corresponding spin. The isodensity value for surfaces is ±0.001 e/au^3. tBu_3 parts are hidden for clarity. The pairs $\Delta\rho_2$, $\Delta\rho_3$ and $\Delta\rho_4$, $\Delta\rho_5$ describe formation of a σ-component of the bond between XyCN and the metal. The last pair $\Delta\rho_6$, $\Delta\rho_7$ also has a π-character.

Figure S21 presents the NOCV contours describing the bond between the $Cr(TBOS_3)_3$ fragment and the two fragments with XyCN ligands in the complex **3**. Eight orbitals participating in bonding exhibit high eigenvalues. $\Delta\rho_1$, $\Delta\rho_2$, $\Delta\rho_3$ corresponding to a σ-component and $\Delta\rho_4$… $\Delta\rho_8$ describing π-components. The lack of ligand-based, antibonding π component suggests the lack of π-backdonation, which is consistent with the observatin in sc-XRD analysis and IR spectroscopy.

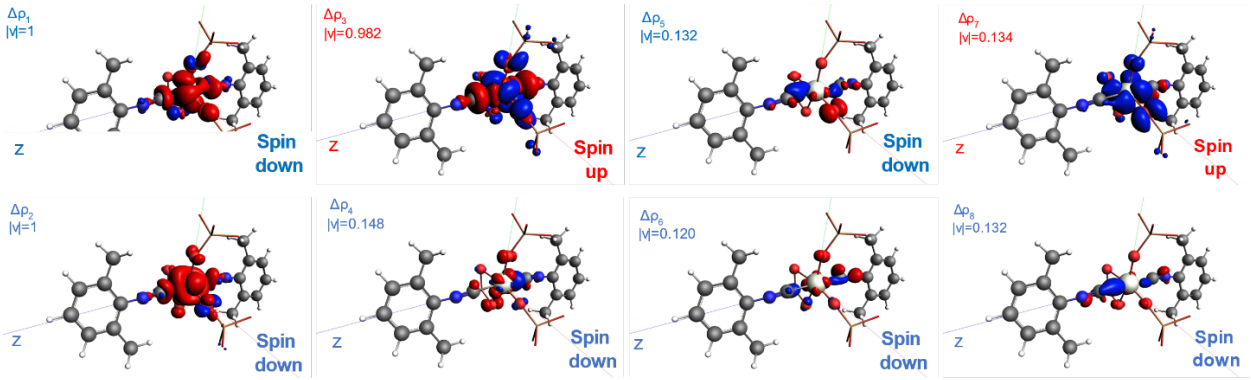

Figure S21. Isosurfaces of the natural orbitals for chemical valence characterizing the bond between the $Cr(TBOS_3)_3$ fragment and two the XyCN ligands fragments with eight highest eigenvalues components (|ν|). The isodensity value for surfaces is ±0.001 e/au^3. tBu_3 parts are hidden.

5. References

1 M. P. Conley, M. F. Delley, G. Siddiqi, G. Lapadula, S. Norsic, V. Monteil, O. V. Safonova and C. Copéret, *Angewandte Chemie - International Edition*, 2014, **53**, 1872–1876.

2 A. Ciborska, J. Chojnacki and W. Wojnowski, *Acta Crystallogr. Sect. E Struct. Rep. Online*, 2007, **63**, m1103–m1104.

3 D. Trummer, K. Searles, A. Algasov, S. A. Guda, A. V. Soldatov, H. Ramanantoanina, O. V. Safonova, A. A. Guda and C. Copéret, *J. Am. Chem. Soc.*, 2021, **143**, 7326–7341.

4 G. R. Fulmer, A. J. M. Miller, N. H. Sherden, H. E. Gottlieb, A. Nudelman, B. M. Stoltz, J. E. Bercaw and K. I. Goldberg, *Organometallics*, 2010, **29**, 2176–2179.

5 D. F. Evans, *J. Chem. Soc.*, 1959, 2003–2005.

6 E. M. Schubert, *J. Chem. Educ.*, 1992, **69**, 62.

7 D. H. Grant, *J. Chem. Educ.*, 1995, **72**, 39.

8 G. A. Bain and J. F. Berry, *J. Chem. Educ.*, 2008, **85**, 532.

9 O. V. Dolomanov, L. J. Bourhis, R. J. Gildea, J. A. K. Howard and H. Puschmann, *J. Appl. Crystallogr.*, 2009, **42**, 339–341.

10 G. M. Sheldrick, *Acta Crystallogr. B*, 2015, **71**, 3–8.

11 B. Ravel and M. Newville, *Phys. Scr.*, 2005, **2005**, 1007.

12 M. Newville, *J. Synchrotron Radiat.*, 2001, **8**, 322–324.

13 D. Gianolio, E. Groppo, J. G. Vitillo, A. Damin, S. Bordiga, A. Zecchina and C. Lamberti, *Chem. Commun.* , 2010, **46**, 976–978.

14 C. Fonseca Guerra, J. G. Snijders, G. te Velde and E. J. Baerends, *Theor. Chem. Acc.*, 1998, **99**, 391–403.

15 J. P. Perdew, K. Burke and M. Ernzerhof, *Phys. Rev. Lett.*, 1996, **77**, 3865–3868.

16 A. D. Becke, *Phys. Rev. A Gen. Phys.*, 1988, **38**, 3098–3100.

17 M. Reiher, O. Salomon and B. Artur Hess, *Theor. Chem. Acc.*, 2001, **107**, 48–55.

18 J. Tao, J. P. Perdew, V. N. Staroverov and G. E. Scuseria, *Phys. Rev. Lett.*, 2003, **91**, 146401.

19 C. Lee, W. Yang and R. G. Parr, *Phys. Rev. B Condens. Matter*, 1988, **37**, 785–789.

20 Y. Zhao and D. G. Truhlar, *Theor. Chem. Acc.*, 2008, **120**, 215–241.

21 S. Grimme, J. Antony, S. Ehrlich and H. Krieg, *J. Chem. Phys.*, 2010, **132**, 154104.

22 S. Grimme, S. Ehrlich and L. Goerigk, *J. Comput. Chem.*, 2011, **32**, 1456–1465.

23 S. A. Guda, A. A. Guda, M. A. Soldatov, K. A. Lomachenko, A. L. Bugaev, C. Lamberti, W. Gawelda, C. Bressler, G. Smolentsev, A. V. Soldatov and Y. Joly, *J. Chem. Theory Comput.*, 2015, **11**, 4512–4521.

24 F. M. Bickelhaupt and E. J. Baerends, in *Reviews in Computational Chemistry*, John Wiley & Sons, Inc., Hoboken, NJ, USA, 2007, pp. 1–86.

25 A. Michalak, M. Mitoraj and T. Ziegler, *J. Phys. Chem. A*, 2008, **112**, 1933–1939.

26 M. Mitoraj and A. Michalak, *J. Mol. Model.*, 2007, **13**, 347–355.

27 G. Bistoni, L. Belpassi and F. Tarantelli, *J. Chem. Theory Comput.*, 2016, **12**, 1236–1244.